

# Fabrication of Metallized Nanopores in Silicon Nitride Membranes for Single-Molecule Sensing

Ruoshan Wei, Daniel Pedone, Andreas Zürner, Markus Döblinger, and Ulrich Rant\*

*The fabrication and characterization of a metallized nanopore structure for the sensing of single molecules is described. Pores of varying diameters (>10 nm) are patterned into free-standing silicon nitride membranes by electron-beam lithography and reactive ion etching. Structural characterization by transmission electron microscopy (TEM) and tomography reveals a conical pore shape with a 40° aperture. Metal films of Ti/Au are vapor deposited and the pore shape and shrinking are studied as a function of evaporated film thickness. TEM tomography analysis confirms metallization of the inner pore walls as well as conservation of the conical pore shape. In electrical measurements of the transpore current in aqueous electrolyte solution, the pores feature very low noise. The applicability of the metallized pores for stochastic sensing is demonstrated in real-time translocation experiments of single  $\lambda$ -DNA molecules. We observe exceptionally long-lasting current blockades with a fine structure of distinct current levels, suggesting an attractive interaction between the DNA and the PEGylated metallic pore walls.*

## Keywords:

- biosensors
- DNA
- nanopores
- nanotechnology
- single-molecule studies

## 1. Introduction

Single nanometer-sized holes in otherwise impervious membranes constitute simple devices to analyze single molecules: when biological macromolecules like DNA or proteins traverse the pore from one side of the membrane to the other, a characteristic signature can be observed in the transpore ionic

current, which represents a footprint of the molecule's size, conformation, charge, or attachment to other molecules.<sup>[1]</sup> In addition to biological pores, artificially fabricated (solid state) nanopore devices have increasingly gained attention,<sup>[2]</sup> not only because of their high stability and ruggedness to environmental conditions but also because of the possibility of engineering the sizes and shapes of the pores. Nanopores have been realized in various materials, including silicon,<sup>[3,4]</sup> silicon nitride,<sup>[5–7]</sup> silicon oxide,<sup>[8,9]</sup> polymers,<sup>[10,11]</sup> aluminum oxide,<sup>[12]</sup> or glass (capillaries),<sup>[13,14]</sup> and a variety of techniques have been used to fabricate the pores, including direct drilling with a tightly focused high-energy electron<sup>[8,9]</sup> or ion beam,<sup>[5,15–17]</sup> shrinking of prepatterned larger openings with a defocused electron or ion beam (“sculpting”),<sup>[12,18]</sup> and ion-track etching techniques.<sup>[7,10]</sup> Apart from the fact that these methods produce orifices with nanometer dimensions, it is important to note that pores of different shapes (e.g., cylindrical,<sup>[19]</sup> conical,<sup>[17]</sup> hour glass<sup>[18,20]</sup>) and chemical compositions are obtained. Engineering the shape and chemical properties of the pore interior is particularly appealing because it allows the pore to be equipped with desired functionalities, for example, to tether designated protein receptors inside the pore<sup>[21,22]</sup> or to mimic biological channels. To this end, it is necessary to coat the inner pore walls, which has been attempted by the self-assembly of

[\*] Dr. U. Rant

Walter Schottky Institut  
Technische Universität München  
Am Coulombwall 3, 85748 Garching (Germany)  
E-mail: rant@wsi.tum.de

R. Wei, D. Pedone  
Walter Schottky Institut  
Technische Universität München  
Am Coulombwall 3, 85748 Garching (Germany)

A. Zürner, Dr. M. Döblinger  
Department of Chemistry  
Ludwig Maximilians-Universität München  
Butenandtstrasse 11, 81377 München (Germany)

Supporting Information is available on the WWW under <http://www.small-journal.com> or from the author.

DOI: 10.1002/smll.201000253

molecular monolayers,<sup>[23–25]</sup> atomic layer deposition (ALD),<sup>[26–29]</sup> electron-beam-induced deposition (EBID),<sup>[4,30,31]</sup> and electroless plating<sup>[24,32,33]</sup> or evaporation<sup>[34–36]</sup> of metals. The latter is especially promising because the well established and versatile thiol chemistry can be used to functionalize metal surfaces; additionally, controlling the electrostatic environment (gating) of the pore becomes easily feasible through the application of external potentials<sup>[29,35,36]</sup> to the metal film in the pore. As the range of applications and use of nanopores as analytical tools grows, it is desirable to have simple fabrication methods available that employ machinery and techniques that are widely accessible.

In this Full Paper, we demonstrate the fabrication of metallized nanopores in SiN membranes with conventional semiconductor process technology, namely e-beam lithography and subsequent vapor deposition of metals. We present the preparation of pores with desired diameters through variation of the e-beam exposure dose and characterize the 3D pore shape by transmission electron microscopy (TEM) tomography. Subsequently, the deposition of thin metal films (Ti/Au) is described and the consequences with respect to the pore diameter and shape are elucidated. Remarkably, the e-beam lithography step produces conical pores and the conical shape is retained even after metal has been deposited. To demonstrate that the device can be used to monitor the translocation of single molecules, we present noise spectra and experiments with  $\lambda$ -DNA in PEGylated pores. The translocation of individual DNA molecules through a metal pore could be observed in real time. In contrast to reports from pores in dielectric materials, the translocation events last for an extremely long time, which suggests a strong attractive interaction of the DNA with the pore.

## 2. Fabrication of Nanopores in SiN Membranes

We employed e-beam lithography to fabricate nanopores with tunable and controllable diameters in a SiN membrane, which was supported by a thick silicon substrate. The process steps are schematically outlined in Figure 1 and described in detail in the Experimental Section. Starting from a single-crystalline (100) silicon wafer with 10-nm SiO<sub>2</sub> and 50-nm low-pressure chemical vapor deposition (LPCVD) Si<sub>3</sub>N<sub>4</sub> layers on both sides, a free-standing SiN membrane was fabricated by conventional microfabrication techniques: a square opening of 270- $\mu$ m side length was created on the backside of the wafer using photolithography and reactive ion etching (RIE). After patterning a resist layer on the wafer front side by e-beam lithography in the dot-exposure mode, an array of nanopores

was etched into the front-side SiN layer by RIE. The SiO<sub>2</sub> spacer layers (omitted for clarity in Figure 1) are etched away during the RIE steps as well. The dot dose during e-beam exposure was adjusted to achieve the desired pore diameter. Finally, an anisotropic wet chemical etching step was carried out in KOH solution to etch away the thick Si layer through the backside opening, which resulted in a large pyramidal cavity (as well as small pyramids on the front side). In so doing, a free-standing SiN membrane containing a single nanopore was created on the front side of the wafer.

A series of dose tests were performed in which pores with various exposure doses were patterned. The resulting pores were imaged by TEM and the pore diameters were analyzed. Figure 2A shows exemplary TEM images of pores of various diameters. The dependence of the pore diameter ( $d_{\text{SiN}}$ ) on the e-beam exposure dose ( $D$ ) plotted in Figure 2B exhibits a monotonic trend, which can be fitted by  $d_{\text{SiN}} = C_0 \cdot D^\gamma$  with  $C_0 = 18.3 \text{ nm}$  and  $\gamma = 0.44$  (dashed line in Figure 2B). These results demonstrate that e-beam lithography is well suited for the fabrication of nanopores with diameters  $>10 \text{ nm}$  with very good reproducibility and straightforward control over the pore diameter.

Compared to other nanopore-preparation methods, like direct drilling or sculpting by TEM or focused ion beam (FIB), the presented fabrication process bears the advantage of high-throughput production. For instance, we usually prepared  $>30$  pores by e-beam lithography within a few hours; all other steps (optical lithography, RIE, KOH etching, and metal evaporation) were processed in parallel, producing a large number of nanopore devices simultaneously. Device-to-device diameter variations were smaller than 3 nm and device yield was above 90%.

Close inspection of the nanopore TEM images reveals that the nanopore orifice is surrounded by a halo-like ring. Across this ring region, the contrast gradually darkens until it reaches the gray value of the SiN membrane. Due to the amorphous nature of SiN, the contrast is dominated by so-called mass-thickness contrast, which is based on elastic Rutherford scattering. Consequently, the specimen thickness can be related to the attenuation of the transmitted intensity by  $\Delta I/I_0 = 1 - e^{-Q\Delta t}$  ( $Q$  is the total elastic scattering cross section depending on the atomic number  $Z$ ;  $\Delta t$  is the thickness change).<sup>[37]</sup> Thus, the bright halo-like ring indicates that the nanopore orifice is surrounded by a membrane region of decreased thickness. Using the exponential intensity-thickness relation, we calculated a thickness profile taking the gray values of the orifice ( $t = 0$ ) and the SiN membrane ( $t_{\text{SiN}} = 50 \text{ nm}$ ) as calibration points. The results are shown in Figure 2C for

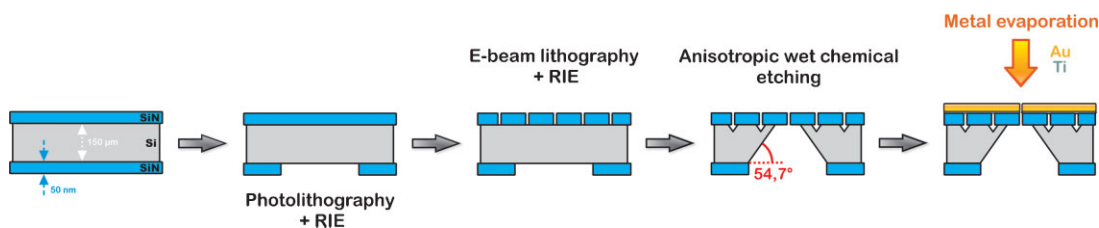
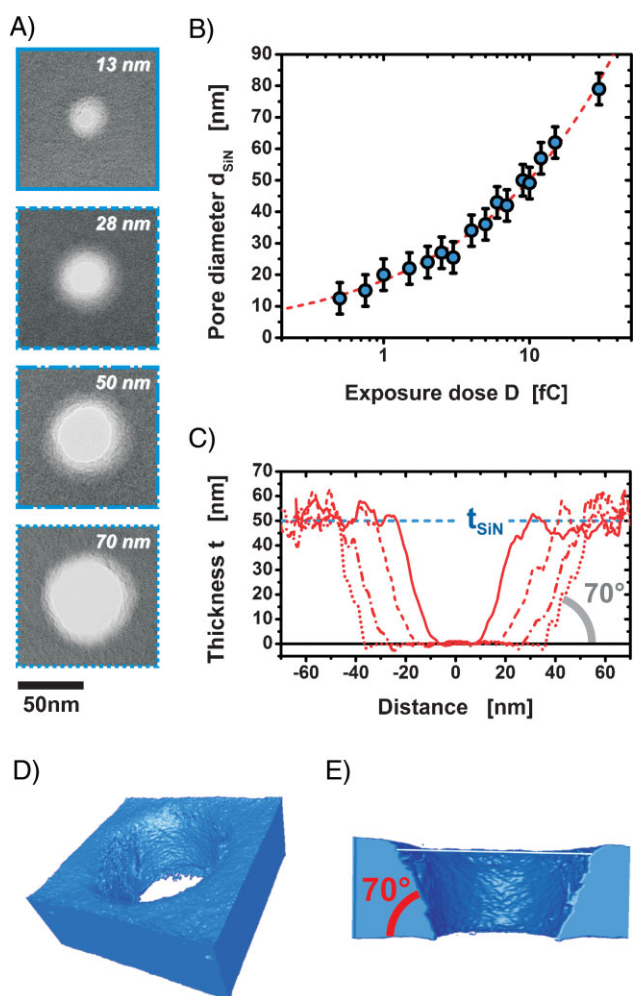


Figure 1. Schematic outline of the nanopore fabrication.



**Figure 2.** A) TEM images of nanopores in SiN membranes of various diameters. B) Pore diameter  $d_{\text{SiN}}$  as a function of e-beam exposure dose  $D$ ; the red dashed line is a fit with  $d_{\text{SiN}} \propto D^2$ . C) Thickness profiles of pores shown in (A) deduced from an intensity analysis. D, E) Electron tomography reconstruction of a SiN nanopore.

exemplary pores in Figure 2A of various diameters. Independent of the pore diameter, we find that the region where the membrane is thinner than the nominal SiN membrane extends roughly 30 nm from the pore edge. Although the plotted thickness profile already suggests a pore shape, the pore geometry cannot be identified unambiguously from this analysis. For instance, pores featuring a conical or hour-glass shape could, in fact, yield the same thickness profile.<sup>[7,18]</sup> For that reason, we investigated the pore shape further by atomic force microscopy (AFM) and TEM tomography.

Electron tomography provides three-dimensional (3D) structural information with nanometer-scale resolution by processing a series of TEM images acquired over different sample-tilt angles. We performed TEM tomography using a FEI Titan 80-300 on a nanopore in a SiN membrane and recorded a single-axis-tilt series of 40 TEM images from  $-40^\circ$  to  $+40^\circ$  with a tilt increment of  $2^\circ$ . A 3D reconstruction computed from a tilt series (see Experimental Section, for further details) is displayed in Figure 2D. The 3D images clearly reveal the shape of a truncated cone. From the cross-sectional view in

Figure 2E, we can extract a sidewall angle of  $71^\circ$ , corresponding to a full aperture of the cone of  $38^\circ$ . Based on the identification of the conical geometry, we can now also infer a sidewall angle from the contrast–thickness analysis (Figure 2C) and find, independent of the pore diameter,  $70^\circ \pm 3^\circ$ , which agrees very well with the tomography analysis. The pore profiles measured by AFM corroborate the conical pore shape; however, details of the height and sidewall angle are obscured due to tip convolution effects (see Supporting Information, Figure S1).

The conical pore shape may result from (a combination of) two processes: (1) nondirectional etching during the RIE step; (2) owing to the undercut profile of the e-beam resist, which results from electrons backscattered from the substrate during the e-beam dot exposure, the regions around the orifice are not fully protected from the plasma during the RIE step (the resist may even become completely ablated) and partial etching occurs.<sup>[38–40]</sup>

### 3. Nanopore Metallization

With the aim of preparing metallic nanopore structures, we deposited metal films on prefabricated SiN nanopores. Thin Au films were evaporated in high vacuum onto the front side of the wafer (c.f. Figure 1), that is, from the side of the large cone opening. Figure 3A shows TEM images of the same nanopores before and after the deposition of 3-nm Ti adhesion layers and 30-nm Au layers, evaporated at a rate of  $(0.7 \pm 0.1) \text{ \AA s}^{-1}$ . Contrary to amorphous SiN membranes, the polycrystalline gold films exhibit strong contrast variations in TEM images, resulting from Bragg reflections of randomly orientated crystalline grains within the Au film (diffraction contrast).

The pore shrinks as a result of the metal deposition. In order to quantify the reduction in pore diameter as function of initial pore size and evaporated metal-film thickness, we metallized a set of SiN pores with initial diameters ranging from 13 to 80 nm with metal films ranging in thickness from 13 to 45 nm. All pores were characterized by TEM before and after the metal deposition; the measured Au-pore diameters,  $d_{\text{Au}}$ , are plotted versus the initial diameter of the SiN pores,  $d_{\text{SiN}}$ , in Figure 3B. Every set of pores with varying  $d_{\text{SiN}}$ , yet fixed metal thickness  $t$  can be fitted by a linear relation  $d_{\text{Au}} = -\Delta d + \alpha \cdot d_{\text{SiN}}$  (dashed lines in Figure 3B). The slope  $\alpha$  is close to unity for all fits; this indicates that the reduction in the pore diameter does *not* depend on the initial diameter  $d_{\text{SiN}}$ . In fact, the pores shrink by a constant value  $\Delta d$ , which depends solely on the evaporated film thickness  $t$ . Figure 3C shows that, for the metal thicknesses studied here, a linear relationship between  $t$  and  $\Delta d$  is observed:  $\Delta d/2 \propto 0.32t$ . The magnitude of the factor 0.32 can be understood by the evaporation geometry. Since the sidewalls of the conical pores are tilted by  $70^\circ$ , it is expected that the flow of Au atoms per area impinging onto the sidewalls is reduced by a factor of  $\cos(70^\circ) = 0.34$ .

When contrasting TEM images of pores metallized with Au films of varying thickness (Figure S2), we observe that pores metallized with very thin films (10 nm) exhibit a discontinuous gold film at the pore opening, while pores with thicker metal films tend to feature grainy pore edges. This is due to the growth mechanism of evaporated thin gold films: first, nucleation of

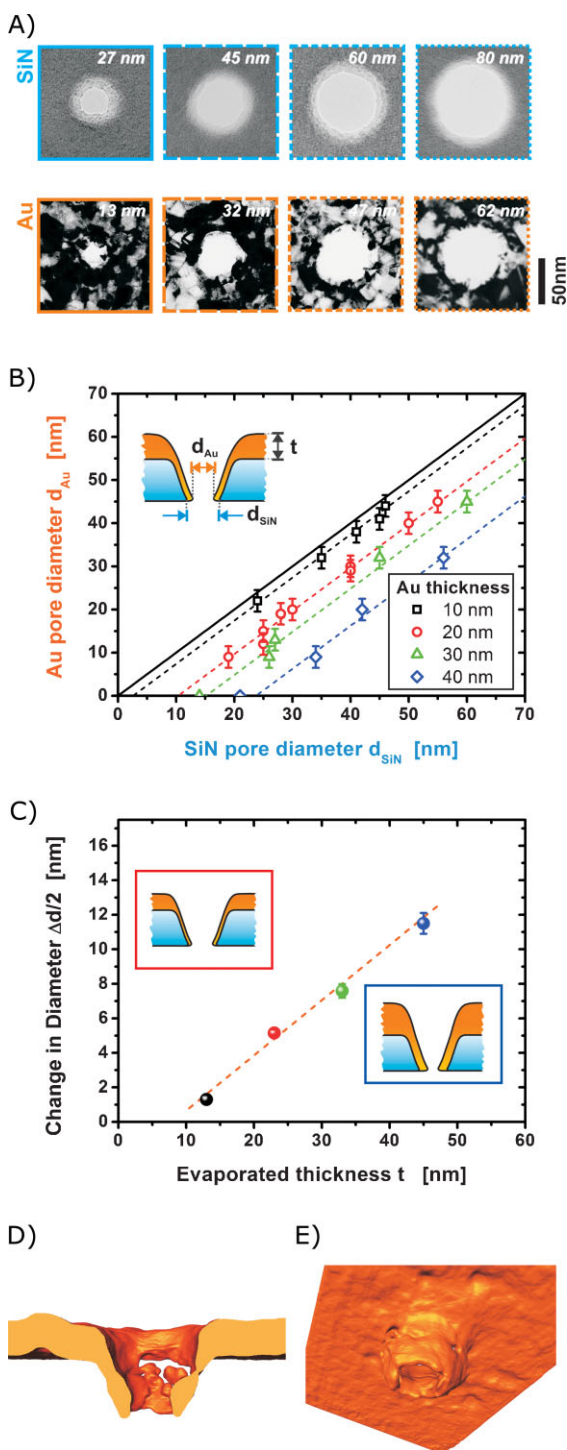


**Figure 3.** A) TEM images of SiN nanopores and the same pores after metallization with 30-nm gold. B) Diameters of various nanopores before ( $d_{\text{SiN}}$ ) and after ( $d_{\text{Au}}$ ) deposition of 10- (black squares), 20- (red circles), 30- (green triangles), and 40-nm (blue diamonds) gold films. Dashed lines are linear fits of unity slope. Errors in the SiN pore-diameter analysis are  $\pm 1$  nm and thus within symbol size. Larger errors ( $\pm 2.5$  nm) occur in the diameter analysis of metallized pores due to the granular structure of the deposited gold film. C) Average change in pore radius as a function of deposited metal thickness. Error bars are deduced from linear fits in panel B. Insets are schematic illustrations of the pore geometry and film thicknesses. D,E) Tomographic reconstructions from a STEM-HAADF series of a nanopore metallized with 20-nm gold.

gold atoms occurs on the substrate surface and the nucleation sites grow in size via impingement or surface diffusion of single atoms, which leads to a discontinuous film consisting of separated gold islands. Upon further metal deposition, the individual islands coalesce and a continuous gold film is formed. Pores metallized with 10- and 20-nm gold could be intermediate stages, where the ultrathin film on the inner pore walls is not yet continuous and thus exhibit voids, which appear as regions of bright contrast in TEM images. For pores metallized with a thicker film, the voids disappear as a continuous film is formed. Owing to the granular growth of the film, the deposition of Au inside the pore also changes the local structure of the pore. We observed that the grain size increased and the pore edges became rougher with increasing metal-film thickness.

To visualize the geometry of a nanopore metallized with a 20-nm Au film, we used scanning TEM in high-angle annular dark field mode (STEM-HAADF). With this method the scattering cross section is approximately proportional to the square of the atomic numbers and the contrast becomes largely independent from the diffraction conditions of the gold crystals.<sup>[41]</sup> Figure 3D and E shows the reconstructed 3D representation obtained from a series of images recorded at different tilt angles. Due to the large difference in atomic numbers between gold and SiN, only the evaporated gold film is visible in the tomographic reconstruction (but not the SiN membrane). The thin gold film coating the inner pore walls can be seen as a funnel extending out of the nearly uniform thicker gold film, which is supported by the membrane. To make the tomographic reconstruction possible, a thin gold film was chosen and, consequently, several voids are visible in the film within the pore region.<sup>[42]</sup> Despite this, most parts of the inner pore wall were coated with gold, albeit only a few nanometers thick. Importantly, the tomography image confirms that the conical pore shape is preserved upon gold deposition.

Excessive metal deposition results in clogging of the pores with metal. Combined analysis of TEM, AFM, and scanning electron microscopy (SEM) imaging from both sides of the wafer revealed that the pores first close at the narrow pore mouth before being “filled up” with Au afterwards (see Figure S3).

Moreover, we found that the final diameter of metallized pores can not only be controlled by the thickness of the evaporated gold film but also by the rate of evaporation. When the metal evaporation was carried out at a high evaporation rate of  $3\text{--}4 \text{ \AA s}^{-1}$ , the pore shrinking was more extreme than for low evaporation rates of  $0.6\text{--}0.8 \text{ \AA s}^{-1}$ . Figure S4 in the Supporting Information compares the pore-diameter reduction after evaporation of 30-nm gold at slow and fast rates. In addition, the data show that, for the high evaporation rate, the pore shrinking actually depends on the initial pore size. Smaller pores shrink faster (i.e., their diameter decreases by as much as 40 nm) than larger pores (their diameter decreases by 16 nm), which is in contrast to the slow evaporation process, for which all pores uniformly shrunk by  $15 \pm 3$  nm, independent of their initial diameter.

#### 4. Electrical Noise

The ability to sense single molecules by the resistive pulse technique (Coulter method)<sup>[43,44]</sup> with a nanopore depends on

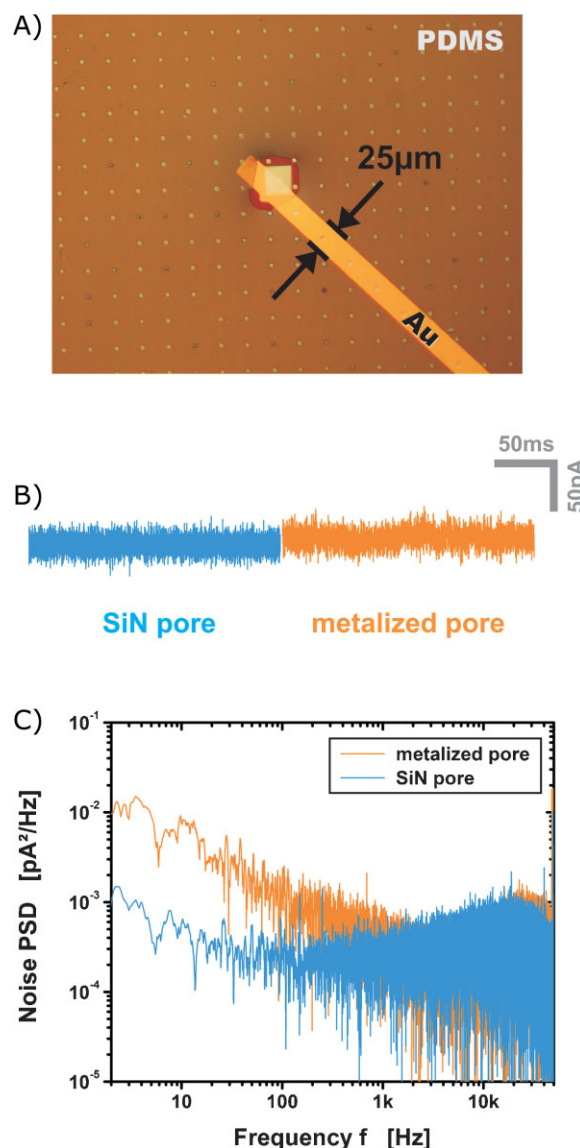
the electrical noise of the device when recording the transpore ionic current, as excessive noise may obscure the low-amplitude current pulses elicited by molecules passing through the pore.  $1/f$  noise, dielectric noise and excess white noise have been identified as the major noise sources in current measurements with solid-state nanopores.<sup>[45–48]</sup> For the detection of short single-molecule translocation events, the high-frequency regime is of particular importance. Here, dielectric noise is the dominating noise source; it arises from the dissipation of energy in nonideal (i.e., lossy) capacitances in the system. Dielectric noise can be reduced by minimizing chip capacitances and dielectric loss of the used materials. Following a protocol by Tabard-Cossa et al.,<sup>[45]</sup> we thus passivated the chip by carefully painting polydimethylsiloxane (PDMS) on the surface, leaving a  $\approx 50\text{-}\mu\text{m}$ -wide window around the nanopore open. Furthermore, we used photolithography to confine the metallized area to a  $25\text{-}\mu\text{m}$ -wide strip in order to reduce capacitive coupling of the metal layer (reference chips with large metal areas were clearly inferior with respect to their noise characteristics). An optical micrograph of the chip is shown in Figure 4A.

Figure 4B shows representative current traces of a SiN pore and a metallized pore (Ti/Au = 5/30 nm) with  $d \approx 35$  nm, which feature comparable root-mean-square current variations of  $I_{rms}^{SiN}(50\text{ mV}) = 15$  pA and  $I_{rms}^{Au}(50\text{ mV}) = 16$  pA, respectively ( $I_{rms}^{SiN}(100\text{ mV}) = 15$  pA;  $I_{rms}^{Au}(100\text{ mV}) = 19$  pA;  $I_{rms}^{Au}(200\text{ mV}) = 26$  pA, data not shown). The noise power spectral density (PSD)  $S^2(f)$  was calculated using a fast Fourier transform (FFT) algorithm from 10-s current-time traces, recorded with a patch-clamp amplifier at a sampling frequency of 200 kHz and 7-pole Bessel-filtered at 30 kHz. The noise spectra mainly differ in the low frequency  $1/f$  noise, where the metallized pore exhibits noise levels that are roughly one order of magnitude higher than the noise of the SiN pore. In general, however, the low-frequency-noise performance of the pores examined in this study is remarkably good compared to other SiN pores<sup>[45,46]</sup> and  $\text{Al}_2\text{O}_3$  pores<sup>[12,26]</sup> reported in the literature (even at 100 mV bias, the noise at  $f = 1$  Hz is only  $0.02\text{ pA}^2\text{ Hz}^{-1}$  and  $0.2\text{ pA}^2\text{ Hz}^{-1}$  for the SiN and metallized pores, respectively). Most importantly, both pore types show minimal dielectric noise in the high-frequency regime ( $f > 1$  kHz), which is a consequence of the low capacitance,  $C$ , of the PDMS passivated chips:  $C$  was analyzed by electrochemical impedance measurements to be  $\approx 30$  pF (c.f. Figure S5).

Current-voltage curves were recorded and are presented in the Supporting Information (Figure S6). The measured pore-resistance values (for instance,  $25\text{ M}\Omega$  for a  $27\text{-nm}$  pore measured in  $400\text{ mM}$  KCl solution) agree well with expectations based on the pore dimensions, indicating that ionic-current transport through the pore is the predominant conductance mechanism.

## 5. DNA Translocation Through Metallized Nanopores

To test whether the metallized nanopore structures can be used for the stochastic sensing of single molecules,<sup>[1,44,49,50]</sup> we conducted DNA translocation experiments. A SiN pore



**Figure 4.** A) Optical micrograph of a PDMS-covered metallized nanopore chip. The metallized Au area (strip) extends across the pore in the chip center. B) Current-time recordings at 50 mV bias voltage of a SiN pore (blue trace) and a metallized pore (5-nm Ti and 30-nm Au; orange trace) and C) the corresponding noise power spectra. Both pores were passivated with PDMS.

( $d = 60$  nm) was metallized with 5-nm Ti and 30-nm Au (resulting diameter  $\approx 35$  nm) and installed in a cell in which it separated two compartments filled with  $1\text{ M}$  KCl solution. The metal layer was left floating during the measurements.  $\lambda$ -DNA was added to the chamber facing the small-cone opening (cis side) and a voltage of  $+215$  mV was applied to the other (trans) side. When the devices were used as fabricated, we usually observed a sudden reduction of the transpore current and the pores remained in the low-current state for minutes thereafter. We attributed this behavior to a partial clogging of the pore by DNA molecules, which presumably strongly adsorbed to the inner pore walls. Thus, we passivated the pore with a self-assembled monolayer (SAM) of PEGylated alkane thiols ( $\text{HS}-(\text{CH}_2)_{15}-(\text{EG})_3-\text{OH}$ ). The surface functionalization of gold

nanopores will be described in detail in an upcoming publication; briefly, thiol-alkane-PEG layers were formed by immersing the pores in 1 mM thiol-alkane-PEG ethanol solutions for 12 h. The successful formation of the monolayer inside the pore was evidenced by the reduction of the transpore current observed in real time and corroborated by electrochemical impedance data. HS-C<sub>15</sub>-EG<sub>3</sub> SAMs could be repeatedly removed from the pores by plasma cleaning and adsorbed again.

After PEGylation of the pore, the translocation of  $\lambda$ -DNA could be observed as transient blockades of the transpore current. Figure 5A shows a representative current-time trace after addition of 2 nM  $\lambda$ -DNA to the cis chamber (controls without DNA were negative). Magnified views of representative current pulses are depicted in Figure 5B–D. Compared to translocation signatures reported in the literature for nonmetallic (SiN,<sup>[51]</sup> SiO<sub>2</sub>,<sup>[52–54]</sup> Al<sub>2</sub>O<sub>3</sub><sup>[12,28]</sup>) solid-state nanopores, the translocation events observed here differ strikingly in shape and duration. Typical pulses of nonmetallic pores are rectangular and last  $\sigma$ (1 ms), while the passage of  $\lambda$ -DNA through Au pores usually exhibits a steep onset during which the current drops within a few milliseconds, followed by a slow recovery (lasting up to several hundred milliseconds) back to the open-pore current. Typical examples of pulses of this kind are shown in Figure 5B and C. Some pulses exhibit a different onset, which lasts considerably longer ( $\sigma$ (100 ms)); a representative example is shown in Figure 5D.

A close inspection of the current pulses reveals that the current changes are not monotonic but instead feature distinct jumps. In order to analyze these jumps in more detail, we examine the current blockage ratio,  $B_r$ , which is defined for every data point as  $B_r = I_{\text{blocked}}/I_{\text{open}}$  ( $I_{\text{blocked}}$  is the reduced ionic current during an event and  $I_{\text{open}}$  is the open-pore current value, i.e., the current baseline). For each translocation event, a baseline  $I_{\text{open}}$  is computed by averaging 1000 data points preceding and following the event. Figure 5E shows a histogram of the blockage ratio from 50 translocation events. At least 7 separate peaks can be clearly identified, which correspond to distinct blockade levels in the current trace. Most importantly, we find that the peaks are equally separated by  $\Delta B_r = (0.56 \pm 0.06)\%$ . The maximal current blockade observed was  $B_r^{\text{max}} \approx 17 \cdot \Delta B_r$ .

A likely explanation for these discrete conductance fluctuations is that the pore lumen gets blocked and unblocked by discrete volume segments. To estimate the blocked volume, we use a simple geometric conductance model as a first approximation. Treating the pore as a cylindrical aperture of length  $l_{\text{pore}} = 85$  nm (50-nm SiN membrane + 35-nm metal) with an effective diameter  $d_{\text{open}}^{\text{eff}} = 40$  nm, the volume of the unblocked pore is  $V_{\text{open}} \approx 1.1 \times 10^5$  nm<sup>3</sup>. Considering the high salinity (1 M KCl) and corresponding short screening length (Debye length = 0.3 nm), we neglect surface effects and assume a homogenous conductivity within the pore. Hence, we obtain for the discrete volume fluctuations  $\Delta V_{\text{blocked}} = \Delta B_r \cdot V_{\text{open}} \approx 600$  nm<sup>3</sup>. It is now interesting to compare  $\Delta V_{\text{blocked}}$  to the excluded volume of a double-stranded DNA segment: the length of a DNA segment that features the same volume is  $l_{\text{DNA}} = 160$  nm, that is, roughly two times the pore length.

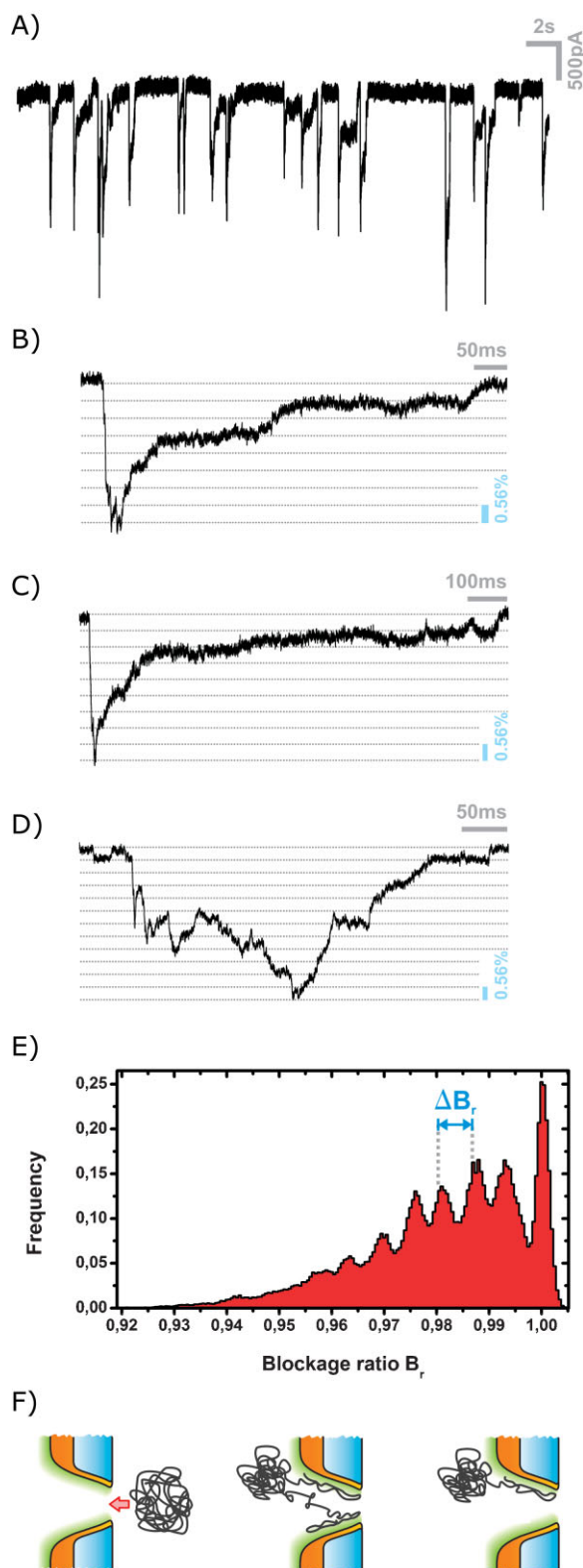


**Figure 5.**  $\lambda$ -DNA translocation through a metallized and PEGylated nanopore. A) Representative current trace at 215 mV transpore bias. B–D) Current-blockage ratio  $B_r = I_{\text{blocked}}/I_{\text{open}}$  versus time for exemplary translocation events. The grid line spacing is chosen according to the characteristic  $\Delta B_r$  value identified from E) the current-blockage-ratio histogram. F) Schematic illustration of the translocation and transient adsorption of a long DNA molecule. The green layer represents the alkane-PEG monolayer, which passivates the gold surface.

Hence, the estimation suggests that the DNA enters and exits the pore in loops.

Although a definite identification of the translocation mode would be premature, we propose the following preliminary interpretation of the translocation behavior: The unusually long residence time of DNA segments inside the pore imply significant attractive interactions between the DNA and the pore walls. This is not unexpected since DNA is known to interact with Au surfaces in multiple ways, in particular through electrostatic<sup>[55]</sup> and “unspecific” (chemical, van der Waals, etc.)<sup>[56]</sup> interactions. Since the latter were minimized by the presence of a PEGylated passivation layer (without the PEGylated SAM, long-term clogging occurred), it seems likely that electrostatic attraction caused the long residence times. Although the potential of the Au pores was not controlled externally in this work, it is possible that a net positive charge was present on the Au surface. Even without being oppositely charged, the metal sidewalls mediate an attractive interaction through induced image charges.<sup>[57,58]</sup> An alternative explanation would be that the pore walls are only partially coated with the PEGylated SAM and “sticky” sites remain on the surface. In any case, eventually, electrophoretic forces are strong enough to shear off the adsorbed DNA from the sidewalls and cause full translocation of the DNA molecule.

Despite the large dimensions of the pore (the pore volume is roughly two times the excluded volume of  $\lambda$ -DNA), the comparably small ratio of the blocked pore volume (<10%) shows that only partial segments of the DNA reside in the pore simultaneously; however, these segments stay in the pore for a long time. The occurrence of distinct current-blockade levels and the estimation of the corresponding blocked volume suggests that the DNA enters and exits the pore in loops, which are probably extracted from a DNA “coil” outside the pore entrance.

## 6. Conclusions

Our results demonstrate that well established semiconductor process technology (e-beam lithography and metal evaporation) can be used to fabricate metallic nanopores with diameters down to  $\approx 10$  nm. An important aspect of the described methods is that the e-beam lithography step produces pores of conical shape in the SiN membrane, so that during the metal-evaporation step, a coating of the inner pore walls is achieved and an “all-metal” device structure (as opposed to a layered structure) is obtained. Not unexpectedly, the metal coating inside the pore was found to be thinner than the evaporated film on the membrane but it is remarkable that the thickness reduction to 1/3 corresponds almost exactly to the geometric expectation for evaporation onto sloped sidewalls. Additionally, for low evaporation rates, the pore shrinking was shown to depend on the deposited metal-film thickness, but not on the initial pore diameter. Thus, the metallization process can be controlled easily and the resulting diameter of the metal pores may be predicted with good accuracy.

The electrical noise of the metallized pores is remarkably low. Hence, the electrical detection of single molecules inside the pore is feasible, as demonstrated in experiments with

$\lambda$ -DNA, where distinct current-blockade levels could be attributed to the entry/exit of individual DNA loops. Interestingly, the passage of DNA through PEGylated metallized pores was found to last significantly longer than through SiN or other dielectric pores, which indicates attractive interactions between the DNA and the pore walls. Despite these attractive interactions, the pore did not become irreversibly clogged by the DNA but eventually electrophoretic forces prevailed in pulling it through the pore. Thus, a pore concept similar to the one presented here might be suited to intentionally slow the DNA translocation, for instance, in attempts to sequence the DNA. Moreover, the presented pore device should be able to be readily gated electrically, following previous reports,<sup>[29,35,36]</sup> and the pore interior can be easily functionalized with SAMs, which will be the subject of further investigations.

## 7. Experimental Section

*SiN nanopore fabrication:* Nanopores were fabricated in 50-nm-thick SiN membranes supported by a thick silicon wafer using e-beam lithography. Polished single crystalline (100) silicon wafer with 10-nm SiO<sub>2</sub> and 50-nm Si<sub>3</sub>N<sub>4</sub> deposited on both sides by LPCVD were purchased from CrysTec GmbH (Germany). Conventional microfabrication techniques were employed to fabricate the SiN membrane: a layer of photoresist (Shipley S1805) was spun onto the backside of the wafer at 10 000 rpm for 40 s and prebaked at 90 °C for 15 min; photolithography created square window patterns (270 × 270  $\mu\text{m}^2$ ) in the photoresist. Following a 30-min postexposure bake at 120 °C, the exposed SiN was removed in a RIE step using CF<sub>4</sub> gas (210-s etch time). The chips were rinsed with acetone and isopropanol and dried in a nitrogen stream prior to the e-beam resist spinning. We used ZEP 520A from Nippon Zeon Co. diluted in anisol (1:1.4 wt%), which was spun onto the frontside (4000 rpm for 99 s) followed by annealing the chips on the hot plate (180 °C, 3 min) to obtain resist-film thicknesses of 90 nm (the thickness was measured on test samples with a DekTak surface profiler). E-beam lithography with the E\_Line system equipped with Elphy Quantum pattern generator from Raith GmbH was used to pattern the nanopores. Exposure was performed at an acceleration voltage of 30 kV with beam currents of  $\approx 20$  pA in the dot exposure mode with typical dot doses from 1 to 25 fC. The patterns were developed in amyl acetate for 1 min, followed by in methyl isobutyl ketone (MIBK) for 10 s and drying in nitrogen. Another RIE step transferred the pattern to SiN. Residual resist was removed after etching by immersion in *N*-methylpyrrolidone (NMP) for 15 min, followed by a deionized (DI) water rinse and drying in nitrogen. Finally, wet chemical etching in aqueous potassium hydroxide (KOH) solution (20 wt%) was carried out at 80 °C to release the SiN membrane.

*Fabrication of metallized nanopores:* Metal-coated nanopores were fabricated using vapor deposition of titanium and gold onto prepatterned SiN pores. The metal deposition was performed in high vacuum ( $< 2 \times 10^{-6}$  Torr) using a Leybold electron beam evaporator. The film thicknesses and evaporation rates were monitored by a quartz crystal microbalance.

For a detailed study of the coating behavior of the inner pore walls with the deposited metal, pores with various sizes were fabricated in SiN membranes and their diameters were inspected by TEM. Next, titanium adhesion layers (3–5 nm) and gold films with thicknesses ranging from 10 to 40 nm were evaporated. Subsequently, the very same pores were once again inspected in TEM. For electrical measurements, instead of evaporating gold onto the whole nanopore chip, we minimized the area of gold on the chip by means of photolithography and liftoff techniques. Photoresist (Shiplot S1805) was spun onto the SiN chip at 10000 rpm for 40 s and prebaked at 90 °C for 15 min; photolithography was used to create a pattern consisting of a 15–25- $\mu\text{m}$ -wide line extending diagonally from the chip center (where the membrane and the pore is situated) to the chip corner. The line terminates in an enlarged square area (1 mm<sup>2</sup>), which will allow electrical contacting of the nanopore in the future. After development of the photoresist, the chip was descummed in an oxygen plasma cleaner for 60 s on both sides in order to remove unwanted photoresist residues. Next, the metal films were evaporated on the photoresist pattern. Subsequent liftoff of the photoresist by immersion in acetone for 20 min resulted in a metallized nanopore chip with a patterned gold area.

**TEM images and tomography:** Plan-view TEM images of the nanopores were taken using a JEOL 100CX with an acceleration voltage of 100 keV. The pore diameters were analyzed using ImageJ software. For electron tomography, TEM and STEM micrographs of the nanopores were recorded with a FEI Titan 80-300 operating at 300 kV. To minimize contributions from diffraction, the camera length in HAADF mode was set to 77 mm. The maximum tilt angle was limited to approximately 40° because of the sample geometry. For the unmetallized SiN pore, a series of TEM images was recorded from –41° to +41°. The metallized pore was imaged in STEM-HAADF mode from –36° to +40°. The projections of each series were aligned by cross correlation using Inspect 3D software from FEI and background corrected using Matlab R2009b (The MathWorks, Inc.). To optimize the resolution and minimize the missing-wedge problem, we used a discrete reconstruction technique (DART).<sup>[59]</sup> The DART algorithm was implemented in a tomography software package written for Matlab, the so called tomography (TOM) toolbox.<sup>[60]</sup> At first a standard simultaneous iterative reconstruction technique (SIRT) reconstruction with at least 20 iterations was performed to obtain a good starting volume for the subsequent DART reconstruction, including at least 50 iterations. Visualization of the resulting 3D data was carried out with Amira 5 (Visage Imaging) by surface rendering.

**Electrical measurements:** For the electrical characterization of nanopores, the chip was sandwiched between two compartments of a custom-built measurement chamber and sealed by soft elastomeric “O rings” with an inner diameter of 0.7 mm. In this way, the nanopore provided the only ionic current path between two reservoirs that were filled with degassed and filtered electrolyte solution (typically 400 mM KCl, adjusted to pH 9 using 10 mM Tris). A bias voltage was applied across the membrane between two homemade Ag/AgCl electrodes that were inserted from the top into the electrolyte. To minimize external noise sources, the whole measurement setup was integrated in a shielded housing and placed on a vibration-isolation table. The

immersed Ag/AgCl electrodes were connected to an EPC8 current amplifier (HEKA, Germany). Immediately before installation into the measurement chamber, the chips were exposed to an oxygen plasma for 30–40 s on both sides in a plasma cleaner (TePla 100-E, Germany) to remove organic contaminants and, importantly, facilitate pore wetting.

**Current-noise analysis:** Current–time traces of the metallized and nonmetallized pores were recorded at constant voltages with the patch-clamp amplifier at a sampling frequency of 200 kHz and a low-pass 7-pole Bessel filter with a cutoff frequency of 30 kHz. The power spectral density  $S^2(f)$  of 10 s of the current noise was obtained by performing FFTs of the recorded current–time traces. Passivation of the chip with PDMS was done manually by carefully thinning out a drop of PDMS around the membrane using a single-loop paint brush attached to a micromanipulator. Subsequently, the chip was cured in an oven at 120 °C for 30 min, resulting in a hardened PDMS layer of  $\approx 10\text{-}\mu\text{m}$  thickness.

**DNA translocation:** Lambda phage DNA (48.5 kbp) was obtained from Fermentas (Germany). The  $\lambda$ -DNA translocation experiments were carried out with the same setup as used in the electrical characterizations. Both chamber compartments were filled with degassed and filtered 1 M KCl solution containing 1 mM EDTA and adjusted to pH 7.5 (10 mM Tris buffer). Current–time traces were recorded with the EPC8 amplifier before and after the addition of 1–2 nM  $\lambda$ -DNA into the chamber facing the small opening of the conical pore at a sampling frequency of 200 kHz and a 5 kHz filter. To passivate the metal pore walls and prevent irreversible DNA adsorption, the metallized pores were coated with a PEGylated SAM of HS-(CH<sub>2</sub>)<sub>15</sub>-EG<sub>3</sub>-OH (1 mM in ethanol solution, 12 h) kindly provided by the group of Prof. Robert Tampé (Goethe University Frankfurt).<sup>[61]</sup>

## Acknowledgements

We are very thankful to Gerhard Abstreiter and Thomas Bein for their support, to Robert Tampé and Christian Grunwald for providing the alkane-PEG and helpful discussions, to Anna Cattani-Scholz for her help with the SAM formation, and to Marianne Hanzlik and Andreas Kastenmüller for their help with plan-view TEM. Financial support is acknowledged from BMBF (0312031A), the TUM Institute for Advanced Studies, DFG via SFB 863, and the Nanosystems Initiative Munich (NIM).

- [1] S. Howorka, Z. Siwy, *Chem. Soc. Rev.* **2009**, *38*, 2360.
- [2] C. Dekker, *Nat. Nanotechnol.* **2007**, *2*, 209.
- [3] S. R. Park, H. B. Peng, X. S. S. Ling, *Small* **2007**, *3*, 116.
- [4] R. Kox, C. Chen, G. Maes, L. Lagae, G. Borghs, *Nanotechnology* **2009**, *20*, 115302.
- [5] J. Li, D. Stein, C. McMullan, D. Branton, M. J. Aziz, J. A. Golovchenko, *Nature* **2001**, *412*, 166.
- [6] A. Han, M. Creus, G. Schurmann, V. Linder, T. R. Ward, N. F. Rooij, U. Staufer, *Anal. Chem.* **2008**, *80*, 4651.
- [7] I. Vlasiouk, P. Y. Apel, S. N. Dmitriev, K. Healy, Z. S. Siwy, *Proc. Natl. Acad. Sci. USA* **2009**, *106*, 21039.

- [8] A. J. Storm, J. H. Chen, X. S. Ling, H. W. Zandbergen, C. Dekker, *Nat. Mater.* **2003**, *2*, 537.
- [9] H. Chang, S. M. Iqbal, E. A. Stach, A. H. King, N. J. Zaluzec, R. Bashir, *Appl. Phys. Lett.* **2006**, *88*, 103109.
- [10] P. Y. Apel, Y. E. Korchev, Z. Siwy, R. Spohr, M. Yoshida, *Nucl. Instrum. Methods Phys. Res. B* **2001**, *184*, 337.
- [11] L. T. Sexton, L. P. Horne, C. R. Martin, *Mol. BioSyst.* **2007**, *3*, 667.
- [12] B. M. Venkatesan, B. Dorvel, S. Yemencioğlu, N. Watkins, I. Petrov, R. Bashir, *Adv. Mater.* **2009**, *21*, 2771.
- [13] J. H. Shim, J. Kim, G. S. Cha, H. Nam, R. J. White, H. S. White, R. B. Brown, *Anal. Chem.* **2007**, *79*, 3568.
- [14] L. J. Steinbock, G. Stober, U. F. Keyser, *Biosens. Bioelectron.* **2009**, *24*, 2423.
- [15] D. M. Stein, C. J. McMullan, J. L. Li, J. A. Golovchenko, *Rev. Sci. Instrum.* **2004**, *75*, 900.
- [16] G. A. T. Chansin, R. Mulero, J. Hong, M. J. Kim, A. J. Demello, J. B. Edel, *Nano Lett.* **2007**, *7*, 2901.
- [17] N. Patterson, D. P. Adams, V. C. Hodges, M. J. Vasile, Michael, P. G. Kotula, *Nanotechnology* **2008**, *19*.
- [18] M. Y. Wu, R. M. M. Smeets, M. Zandbergen, U. Ziese, D. Krapf, P. E. Batson, N. H. Dekker, C. Dekker, H. W. Zandbergen, *Nano Lett.* **2009**, *9*, 479.
- [19] L. Petrossian, S. J. Wilk, P. Joshi, S. Hihath, J. D. Posner, S. M. Goodnick, T. J. Thornton, *Solid-State Electron.* **2007**, *51*, 1391.
- [20] M. J. Kim, B. McNally, K. Murata, A. Meller, *Nanotechnology* **2007**, *18*, 205302.
- [21] Z. Siwy, L. Trofin, P. Kohli, L. A. Baker, C. Trautmann, C. R. Martin, *J. Am. Chem. Soc.* **2005**, *127*, 5000.
- [22] M. Ali, B. Yameen, R. Neumann, W. Ensinger, W. Knoll, O. Azzaroni, *J. Am. Chem. Soc.* **2008**, *130*, 16351.
- [23] K. B. Jirage, J. C. Hulteen, C. R. Martin, *Anal. Chem.* **1999**, *71*, 4913.
- [24] L. T. Sexton, L. P. Horne, S. A. Sherrill, G. W. Bishop, L. Baker, C. R. Martin, *J. Am. Chem. Soc.* **2007**, *129*, 13144.
- [25] M. Wanunu, A. Meller, *Nano Lett.* **2007**, *7*, 1580.
- [26] P. Chen, T. Mitsui, D. B. Farmer, J. Golovchenko, R. G. Gordon, D. Branton, *Nano Lett.* **2004**, *4*, 1333.
- [27] A. H. Talasaz, Y. Liu, M. Ronaghi, R. W. Davis, *Conf. Proc. IEEE Eng. Med. Biol. Soc.* **2006**, *1*, 1830.
- [28] Y. R. Kim, J. Min, I. H. Lee, S. Kim, A. G. Kim, K. Kim, K. Namkoong, C. Ko, *Biosens. Bioelectron.* **2007**, *22*, 2926.
- [29] S. W. Nam, M. J. Rooks, K. B. Kim, S. M. Rossnagel, *Nano Lett.* **2009**, *9*, 2044.
- [30] J. Nilsson, J. R. I. Lee, T. V. Ratto, S. E. Letant, *Adv. Mater.* **2006**, *18*, 427.
- [31] C. Danelon, C. Santschi, J. Brugger, H. Vogel, *Langmuir* **2006**, *22*, 10711.
- [32] C. R. Martin, M. Nishizawa, K. Jirage, M. Kang, *J. Phys. Chem. B* **2001**, *105*, 1925.
- [33] I. Lokuge, X. Wang, P. W. Bohn, *Langmuir* **2007**, *23*, 305.
- [34] B. C. Gierhart, D. G. Flowitz, S. J. Chen, Z. Zhu, Kotecki, R. L. Smith, S. D. Collins, *Sens. Actuators B* **2008**, *132*, 593.
- [35] M. Taniguchi, M. Tsutsui, K. Yokota, T. Kawai, *Appl. Phys. Lett.* **2009**, *95*, 123701.
- [36] E. B. Kalman, O. Sudre, I. Vlassioux, Z. S. Siwy, *Anal. Bioanal. Chem.* **2009**, *394*, 413.
- [37] M. De Graef, *Introduction to Conventional Transmission Electron Microscopy*, Cambridge University Press, Cambridge, UK **2003**.
- [38] A. A. Tseng, K. Chen, C. D. Chen, K. J. Ma, *IEEE Trans. Electron. Packag. Manuf.* **2003**, *26*, 141.
- [39] R. Colombelli, K. Srinivasan, M. Troccoli, O. Painter, C. Gmachl, D. M. Tennant, A. Sergent, D. L. Sivco, A. Y. Cho, F. Capasso, *Nanotechnology* **2004**, *15*, 675.
- [40] Y. S. Peng, B. Xu, X. L. Ye, J. B. Niu, R. Jia, Z. G. Wang, *Opt. Quant. Electron.* **2009**, *41*, 151.
- [41] P. Rez, *Microsc. Microanal.* **2001**, *7*, 356.
- [42] J. E. Morris, T. J. Coutts, *Thin Solid Films* **1977**, *47*, 3.
- [43] H. Bayley, C. R. Martin, *Chem. Rev.* **2000**, *100*, 2575.
- [44] R. R. Henriquez, T. Ito, L. Sun, R. M. Crooks, *Analyst* **2004**, *129*, 478.
- [45] V. Tabard-Cossa, D. Trivedi, M. Wiggin, N. N. Jetha, A. Marziali, *Nanotechnology* **2007**, *18*, 6.
- [46] R. M. M. Smeets, U. F. Keyser, N. H. Dekker, C. Dekker, *Proc. Natl. Acad. Sci. USA* **2008**, *105*, 417.
- [47] J. D. Uram, K. Ke, M. Mayer, *ACS Nano* **2008**, *2*, 857.
- [48] D. P. Hoogerheide, S. Garaj, J. A. Golovchenko, *Phys. Rev. Lett.* **2009**, *102*, 4.
- [49] J. J. Kasianowicz, E. Brandin, D. Branton, D. W. Deamer, *Proc. Natl. Acad. Sci. USA* **1996**, *93*, 13770.
- [50] S. G. Lemay, *ACS Nano* **2009**, *3*, 775.
- [51] D. Fologea, E. Brandin, J. Uplinger, D. Branton, J. Li, *Electrophoresis* **2007**, *28*, 3186.
- [52] A. J. Storm, C. Storm, J. H. Chen, H. Zandbergen, J. F. Joanny, C. Dekker, *Nano Lett.* **2005**, *5*, 1193.
- [53] A. J. Storm, J. H. Chen, H. W. Zandbergen, C. Dekker, *Phys. Rev. E* **2005**, *71*, 051903.
- [54] R. M. M. Smeets, U. F. Keyser, D. Krapf, M. Y. Wu, N. H. Dekker, C. Dekker, *Nano Lett.* **2006**, *6*, 89.
- [55] M. Erdmann, R. David, A. Fornof, H. E. Gaub, *Nat. Nanotechnol.* **2010**, *5*, 154.
- [56] H. Kimura-Suda, D. Y. Petrovykh, M. J. Tarlov, L. J. Whitman, *J. Am. Chem. Soc.* **2003**, *125*, 9014.
- [57] A. V. Dobrynin, M. Rubinstein, *Prog. Polym. Sci.* **2005**, *30*, 1049.
- [58] R. R. Netz, D. Andelman, *Phys. Rep.* **2003**, *380*, 1.
- [59] K. J. Batenburg, S. Bals, J. Sijbers, C. Kubel, P. A. Midgley, J. C. Hernandez, U. Kaiser, E. R. Encina, E. A. Coronado, G. Van Tendeloo, *Ultramicroscopy* **2009**, *109*, 730.
- [60] S. Nickell, F. Forster, A. Linaroudis, W. Del Net, F. Beek, R. Hegerl, W. Baumeister, J. M. Plitzko, *J. Struct. Biol.* **2005**, *149*, 227.
- [61] A. Tinazli, J. L. Tang, R. Valiokas, S. Picuric, S. Lata, J. Piehler, B. Liedberg, R. Tampe, *Chem. Eur. J.* **2005**, *11*, 5249.

Received: February 16, 2010  
Revised: April 20, 2010  
Published online: June 17, 2010